

Article

Effect of Co-Reduction Conditions of Nickel Laterite Ore and Red Mud on Ferronickel Particle Size Characteristics and Grindability of Carbothermic Reduction Products

Xiaoshuang Guo, Zhengyao Li *, Zijun Wang and Tichang Sun

School of Civil and Resource Engineering, University of Science and Technology Beijing, Beijing 100083, China; b20190039@xs.ustb.edu.cn (X.G.); wangzj@ustb.edu.cn (Z.W.); suntc@ces.ustb.edu.cn (T.S.)

* Correspondence: zyli0213@ustb.edu.cn

Abstract: The carbothermic co-reduction of nickel laterite ore and red mud realized the simultaneous reduction of nickel, iron in laterite ore, and iron in red mud at high efficiency. Nickel and iron in nickel laterite ore and iron in red mud were recovered in the form of ferronickel. The size characteristics of ferronickel particles and grindability of carbothermic reduction products are essential for obtaining good technical indicators. The influence of co-reduction conditions on ferronickel particle size and relative grindability was investigated by a carbothermic reduction test, particle size analysis, and relative grindability determination. The mean size of ferronickel particles increased and the proportion of coarse particles grew with improving carbothermic reduction temperature, increasing appropriately anthracite dosage, and prolonging carbothermic reduction time. However, the relative grindability of carbothermic reduction products deteriorated when reduction temperature was improved and the reduction time was extended. The relative grindability was negatively correlated to the ferronickel particle size. The carbothermic reduction temperature had the most dominant effect on the ferronickel particle size and relative grindability, followed by the anthracite dosage and reduction time. More nickel-bearing and iron-bearing minerals were reduced to metallic state with raising reduction temperature and increasing appropriate anthracite dosage. The fine ferronickel particles agglomerated and merged into bulk ferronickel grains with a prolonged reduction time. The results will provide theoretical guidance for the recovery of nickel and iron by co-reduction of nickel laterite ore and red mud.

Keywords: co-reduction; ferronickel particle; size characteristics; relative grindability



Citation: Guo, X.; Li, Z.; Wang, Z.; Sun, T. Effect of Co-Reduction Conditions of Nickel Laterite Ore and Red Mud on Ferronickel Particle Size Characteristics and Grindability of Carbothermic Reduction Products. *Minerals* **2022**, *12*, 357. <https://doi.org/10.3390/min12030357>

Academic Editor:
Konstantinos Komnitsas

Received: 5 February 2022

Accepted: 13 March 2022

Published: 15 March 2022

Publisher's Note: MDPI stays neutral with regard to jurisdictional claims in published maps and institutional affiliations.



Copyright: © 2022 by the authors. Licensee MDPI, Basel, Switzerland. This article is an open access article distributed under the terms and conditions of the Creative Commons Attribution (CC BY) license (<https://creativecommons.org/licenses/by/4.0/>).

1. Introduction

Nickel is a silver-white ferromagnetic metal with a melting point of 1455 °C. It has good corrosion resistance and oxidation resistance and has good mechanical strength and ductility at low temperatures [1]. Nickel is used to produce stainless steel, high-temperature alloys and special alloys with high performance, nickel-cobalt alloys, and nickel-based sputtering materials [2,3]. The excellent physical and chemical properties of nickel-metal determine that it can be widely used in hundreds of thousands of products. In 2021, global nickel mine production reached 2.7 million tons of metal, an increase of 8% from 2020 (2.51 million tons). Indonesia's nickel mine production reached 1 million tons of metal, followed by the Philippines (370,000 tons) and Russia (250,000 tons).

There are two types of nickel ore deposits, namely laterite and sulfide ores [4]. In the distribution of nickel ore resources in the world, nickel laterite ore accounts for about 60%, sulfide nickel ore accounts for 28%, and nickel in seabed iron-manganese nodules accounts for 12% [5,6]. Due to factors such as mining technology and environmental protection, the seabed ferromanganese nodules have not yet been developed. The extraction of nickel from nickel sulfide ore has the advantage of low cost, so it is prioritized and continuously mined by manufacturers, resulting in less and less nickel sulfide resource reserves, showing a

rapid downward trend. Due to the reduction of nickel sulfide ore resources, the world's demand for nickel is increasing, and producers have shifted their nickel production focus to nickel laterite ore. Nickel laterite ore has the advantages of shallow burial and low mining cost. The growth of nickel laterite ore production is more obvious than that of nickel sulfide ore. Nickel laterite ore accounted for about 57% of nickel ore supply in 2007, and this proportion has increased to 64% by 2017. Therefore, nickel laterite ore has become the raw material for nickel extraction [7].

According to the different components, nickel laterite ore can be divided into two categories: silicon-magnesium-nickel type and limonite type [8]. Silicon-magnesium-nickel laterite nickel ore is characterized by relatively high silicon and magnesium content, low iron content and low cobalt content. Limonite-type laterite nickel ore is characterized by high iron content, low nickel content, and low silicon and magnesium content. There are two main methods for the treatment of limonite-type laterite nickel ore: wet treatment and fire treatment [9]. The wet treatment process mainly includes atmospheric pressure acid leaching [10–12] and high-pressure acid leaching [13,14]. Atmospheric pressure acid leaching has the advantages of simple process, high nickel leaching rate, low equipment cost, and short construction period, but it has the disadvantages of having a slow leaching speed, difficult solid-liquid separation, high iron content in leaching solution and a difficult to handle [9]. The pressurized acid leaching method is also called the HPAL process. Compared with normal pressure acid leaching, when nickel laterite ore is acid leached under pressure, the reaction rate is accelerated, nickel and cobalt remain in the leaching solution as valuable ions, and the impurities undergo hydrolysis reaction to form the leaching solution. Precipitation in the form of precipitation, the recovery of nickel and cobalt obtained is usually 90% to 95%. The pressurized acid leaching process can selectively leach nickel from laterite nickel ore and has the advantages of fast reaction speed and low process cost. However, the production process is complex, requires high equipment quality, consumes a large number of reagents, and is not easy to meet the environmental protection standards. Rotary kiln drying and pre-reduction-reduction smelting by the electric furnace (RKEF) is a typical pyrolysis process for nickel laterite ore [15]. The advantage is that the smelting is at a higher temperature, the gas environment in the furnace is better controlled, and it is easy to achieve production expansion. However, there are also problems such as long process flow and high cost, which are easy to cause environmental pollution and difficult to effectively recover other heavy metals. The sintering-blast furnace sulfidation smelting method is suitable for processing laterite nickel ore with nickel content exceeding 1%. Compared with the RKEF process, it has the advantages of simple process, simple operation, low energy consumption, etc., and can recover heavy metals such as cobalt. However, the nickel recovery of this process is relatively low, the magnesium content is strictly required, and the environmental protection pressure is large. Scholars have developed a direct reduction-magnetic separation process on the basis of the pyrotechnic process [16]. The process is to directly reduce the valuable metal oxides in laterite nickel ore with a reducing agent (mostly carbon powder), and obtain nickel-iron alloy through reduction and magnetic separation. The direct reduction-magnetic separation recovery nickel-iron alloy process has high efficiency. Compared with the traditional fire process, it does not need to heat all the laterite nickel ore to a molten state, and the energy consumption is low. The processes are suitable for the recovery of nickel from a low-grade laterite ore with short process, simple technology, and high production efficiency [17]. Additionally, the addition of alkali compounds, such as sodium or calcium salts, could speed up the reduction reaction of nickel and iron oxide, and promote the growth of ferronickel particles [18–20]. However, the addition of sodium or calcium salts such as Na_2CO_3 , Na_2SO_4 , CaF_2 , CaO also led to an increase in carbothermic reduction costs because of their high prices [21]. Therefore, it was necessary to find low-cost alternatives to replace sodium or calcium salts.

Red mud, also called bauxite residue, is the main waste produced during the alumina production process [22,23]. Red mud from the Bayer process is mainly composed of a mixture of oxides such as Fe_2O_3 , SiO_2 , Al_2O_3 , CaO , Na_2O . Red mud is highly alkaline

(pH 10.5–11.0) due to its high content of CaO and Na₂O [24,25]. Therefore, the disposal and storage of the red mud have been a great challenge [26,27]. However, red mud contains more iron minerals and has great potential as an available secondary resource in iron recovery.

According to the high content of CaO and Na₂O of the red mud, researchers recently proposed to use the red mud to replace the sodium or calcium salts added in the reduction of nickel laterite ore [28]. The research results indicated that CaO and Na₂O in red mud promoted the reduction of nickel and iron minerals in nickel laterite ore, and reduced the melting point of the system, which was conducive to the growth of nickel and iron particles [29]. Through co-reduction of nickel laterite ore and red mud, the simultaneous reduction of nickel, iron in laterite ore and iron in red mud at high efficiency were realized [30]. In this process, nickel and iron minerals in laterite ore were reduced to metallic nickel and metallic iron, respectively, iron minerals in red mud were reduced to metallic iron, and metallic nickel was gathered to ferronickel particles based on metallic iron acting as a carrier [31]. In other words, nickel and iron in nickel laterite ore and iron in red mud were recovered in the form of ferronickel. Through the co-reduction-magnetic separation process of nickel laterite ore and red mud, a ferronickel product with a nickel grade of 1.98%, iron grade of 87.98%, nickel recovery of 99.54% and iron recovery of 95.59% was obtained [32]. The advantages of the co-reduction method included efficient recovery of nickel and iron, self-supply of alkaline metal compounds by red mud, red mud resource utilization, and production cost reduction [33].

The effectiveness of the co-reduction process is highly dependent on the ease of separation of ferronickel particles from the gangue phases in the ore because large particles will separate easily using a magnetic separator from surrounding impurities [34]. Therefore, the formation and growth of ferronickel particles are essential in the co-reduction processes. However, previous research focused on the effects of carbothermic reduction conditions on the grades and recoveries of nickel and iron in the ferronickel product during the co-reduction process. For example, Wang found that adding the red mud and anthracite at a suitable dosage was favorable to the reduction of the laterite ore, and the comprehensive recovery of iron in the red mud was achieved [35]. Guo found that a high reduction temperature was conducive to increasing the recoveries of nickel and iron [36]. In particular, the quality of the ferronickel product after magnetic separation was described roughly by the relative size of the ferronickel particle size in the SEM image rather than systematic and detailed analysis [33]. However, how co-reduction conditions affect the grindability and ferronickel particle size characteristics of co-reduction products has not been reported yet. Moreover, the mechanism of co-reduction of nickel laterite ore and red mud remains unclear.

Therefore, in this work, the factors affecting the grindability and ferronickel particle size characteristics during co-reduction of nickel laterite ore and red mud were investigated by carbothermic reduction condition test, particle size analysis, and relative grindability determination. The co-reduction mechanism was analyzed by mineral transformation, magnetic properties, and microstructure. It is expected that the present research will provide theoretical guidance for optimization parameters of co-reduction of nickel laterite ore and red mud.

2. Materials and Methods

2.1. Materials

The nickel laterite ore from Indonesia and red mud were collected from Shanxi province, China. They were crushed to powder fully below 2 mm by using a roll crusher.

Chemical analysis results of the nickel laterite ore and red mud were shown in Table 1. The concentrations of Ni, TFe, SiO₂, Al₂O₃ in the nickel laterite ore were 1.09 wt%, 46.11 wt%, 4.84 wt%, and 6.98 wt%, respectively. The content of iron was relatively high, and the content of silica was relatively low, indicating that it was limonite-type nickel laterite ore [37,38]. In addition, red mud contained 36.27 wt% TFe, 7.78 wt% SiO₂ and 10.68 wt% Al₂O₃.

Table 1. Results of the main chemical element/oxide analysis on the laterite ore and red mud (wt%).

Element/Oxide	Ni	TFe	CaO	Na ₂ O	MgO	MnO	TiO ₂	Al ₂ O ₃	SiO ₂	S
Laterite ore	1.09	46.11	0.04	-	1.67	1.85	0.19	6.98	4.84	0.05
Red mud	-	36.27	0.73	3.83	1.10	-	5.24	10.68	7.78	-

The X-ray diffraction (XRD, Rigaku D/Max 2500, Tokyo, Japan) patterns of nickel laterite ore and red mud revealed that the nickel laterite ore was mainly composed of iron-bearing minerals, including goethite and hematite (Figure 1a). No nickel-bearing mineral phase was detected due to its low concentration. The main crystalline phases present in red mud were hematite, quartz, and sillimanite (Figure 1b).

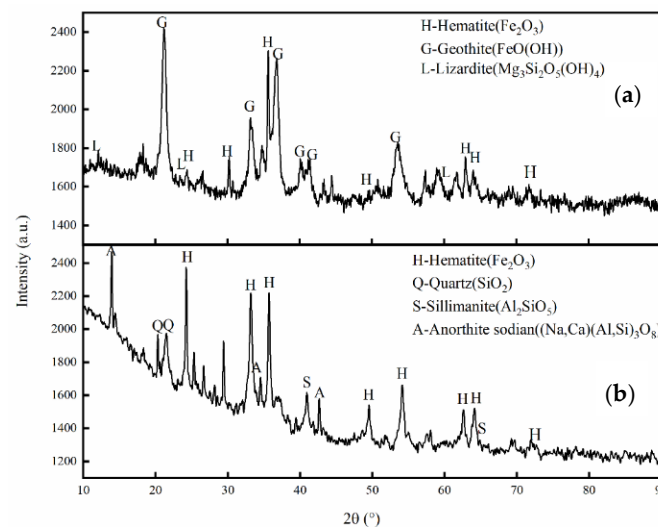


Figure 1. XRD patterns of raw materials: (a) nickel laterite ore; (b) red mud.

The reductant was anthracite with a particle size of less than 1 mm, in which the fixed carbon was 63.90 wt%, ash was 23.25 wt%, the volatile matter was 11.69 wt%, and moisture was 1.17 wt%.

2.2. Experimental Approach

The specific process flowsheet is shown in Figure 2 and the operation process was as follows.

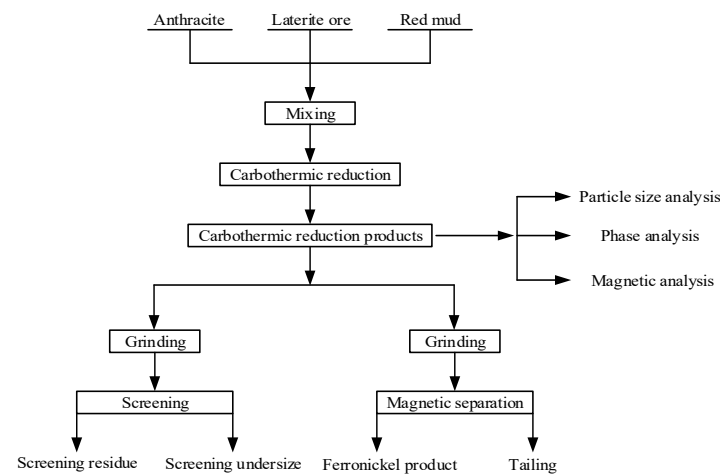


Figure 2. Process flowsheet.

(1) Nickel laterite ore (48 g), red mud (12 g), and anthracite (12 wt%–24 wt% based on 60 g) were mixed manually and thoroughly. (2) The mixed sample was placed in a corundum crucible (50 mm in diameter and 70 mm in height). The crucible was placed in the shaft furnace after the shaft furnace reached the designated temperature and $5 \text{ L} \cdot \text{min}^{-1}$ of N_2 was introduced to remove the air in the shaft furnace. It was kept in a given time ranging from 10 min to 90 min. After that, the co-reduction product was cooled naturally. (3) The carbothermic reduction product was blended fully to obtain the representative sample. The phase analysis, particle size analysis and magnetic analysis of the carbothermic reduction product were carried out. The metallization degree of nickel and iron was determined. (4) The carbothermic reduction product was weighted 40 g for grinding and subsequent screening processes. The particle size characteristics of the reduction product were obtained. (5) The reduction product was subjected to two-stage grinding and two-stage magnetic separation. The first stage grinding fineness and the second stage grinding fineness were $-0.074 \text{ mm } 80\%$ and $-0.043 \text{ mm } 75\%$ respectively. The magnetic field strength of the two stages of magnetic separation was $96 \text{ kA} \cdot \text{m}^{-1}$. The resulting magnetic product was called the ferronickel product.

In order to seek the optimal experimental condition and the major parameters in the co-reduction and grinding processes, an $L_{16}(4^5)$ orthogonal experiment was carried out based on the results of the single-factor experiments.

2.3. Analytical Methods

Grindability, a property used to describe the difficulty of solid particles being ground, is considered one of the important variables in the co-reduction process and is usually characterized by a Bond Work Index [39] or relative grindability. Relative grindability means grinding the ores for the same amount of time, the finer contents account for, the easier the ore is to be ground. The carbothermic reduction product was weighted 40 g. Grinding time was 10 min and grinding concentration was 66.7% treated by an RK/BM-1.0 L rod mill. A sieve with a mesh size of 0.074 mm was performed on a wet vibrating screen, which sifted for 10 min with a 388 Hz vibration frequency. Since there is no standard for the relative grindability of the co-reduction products of nickel laterite ore and red mud, the relative grindability (G) in this paper could be defined as follows:

$$G = \frac{M_r}{M_s} \quad (1)$$

where M_r is the mass fraction of the co-reduction product (-0.074 mm); M_s is the mass fraction of the co-reduction product at $1400 \text{ }^\circ\text{C}$ for 90 min with 16 wt% anthracite (-0.074 mm); M_r and M_s are obtained at the same grinding and screening conditions.

Fe was determined by potassium dichromate ($\text{K}_2\text{Cr}_2\text{O}_7$) titration. 0.15~0.25 g sample was weighed, placed in a 250 mL conical flask, wet with a small amount of water. 15 mL of concentrated HCl solution was added, and the sample was decomposed by heating at a low temperature. After the sample was completely decomposed, a 50 g/L SnCl_2 solution was added with a dropper. 20 mL of distilled water was added and the solution was cooled to room temperature. 10 mL HgCl_2 solution was added, and it was left for 3~5 min to complete the reaction. The test solution was diluted to 150 mL with distilled water, 15 mL of sulfur-phosphorus mixed acid was added, and 4~6 drops of sodium diphenylamine sulfonate indicator were added. The test solution was titrated with $\text{K}_2\text{Cr}_2\text{O}_7$ standard solution until the solution was stable purple, which was the endpoint. The mass fraction of iron was calculated based on the volume of $\text{K}_2\text{Cr}_2\text{O}_7$ standard solution consumed. Ni was determined by the ICP-OES method. 0.1~0.2 g of sample was weighed and placed in a 100 mL polytetrafluoroethylene beaker, and a small amount of water was added to wet it. 5 mL of HF and 10 mL of HNO_3 were added, and the solution was heated on an electric furnace with an asbestos plate until the solution was nearly dry. Then, 2 mL of perchloric acid was added to smoke to drive off fluorine, and then evaporated to near dryness. 5 mL of HCl (1:1) was added to dissolve the sample, 50 mL of hot distilled water

was added to dissolve the soluble salts, and cooled to room temperature. The solution was transferred into a 100 mL volumetric flask, diluted to the mark, shaken up, and measured by ICP-OES (ThermoFisher iCAP7000). The iron and nickel metallization degree was calculated according to the following Equations (2) and (3):

$$\eta_{\text{Fe}} = \frac{\text{MFe}}{\text{TFe}} \times 100\% \quad (2)$$

where η_{Fe} is the iron metallization degree (%), MFe is the mass content of metallic iron of the carbothermic reduction products (%), and TFe is the total iron grade of the carbothermic reduction products (%).

$$\eta_{\text{Ni}} = \frac{\text{MNi}}{\text{TNi}} \times 100\% \quad (3)$$

where η_{Ni} is the nickel metallization degree (%), MNi is the mass content of metallic nickel of the carbothermic reduction products (%), and TNi is the total nickel grade of the carbothermic reduction products (%).

Two samples were simultaneously roasted for each condition to perform a mechanistic study. One of the carbothermic reduction products was prepared into powder to identify the mineral transformations. The XRD experiments were carried out on a Japan Science Ultima IV diffractometer using a Cu target. The magnetic intensities of raw materials and reduction products were analyzed with a JDAW-2000D vibrating sample magnetometer with a magnetic field range of 40–1200 kA/m and magnetic moment range of 0–140 at a vibration head frequency of 180 Hz.

The microstructure and particle size were determined by a BGRIMM (Beijing General Research Institute of Mining & Metallurgy) process mineralogy analyzer (BPMA). The BPMA is conducted in BGRIMM. A BPMA was equipped with a scanning electron microscope (SEM), advanced energy dispersive spectrometer, and software developed by BGRIMM. The reduced samples were dispersed in epoxy resin to obtain several dishes. The dishes were polished to expose the metallic ferronickel particle surfaces. Then, the samples were photographed using a SEM and an acquired image included bright ferronickel particles distributed in a grey background. Afterwards, the captured images were processed with the help of software systematically distinguishing different mineral phases based on a backscattered electron image.

The particle size analysis is an important tool to gain a better understanding of particle growth. The size characteristics of the ferronickel particles in the carbothermic reduction products were measured using BPMA analysis automatically. Cross-sectional areas of more than 5000 ferronickel particles in each carbothermic reduction product were counted. The data on the diameter and numbers of the ferronickel particles were exported to an Excel spreadsheet for further analysis. The equivalent diameter of each metallic ferronickel particle can be calculated using Equation (4).

$$D_i = 2\sqrt{\frac{S_i}{\pi}} \quad (4)$$

where D_i is the equivalent diameter of each measured metallic ferronickel particle, μm ; and S_i is the cross-sectional area of the corresponding metallic ferronickel particle, μm^2 .

Furthermore, the mean size was calculated by Equation (5) to investigate the effect on the growth behavior of ferronickel particles. In this formula, the weighted cross-sectional area method was carried out to weaken the mass impacts of small particles.

$$D = \frac{\sum_1^N D_i S_i}{\sum_1^N S_i} \quad (5)$$

where D is the mean size, μm ; D_i is the equivalent diameter of each measured metallic ferronickel particle, μm ; S_i is the cross-sectional area of the corresponding metallic ferronickel particle, μm^2 ; and N is the total number of ferronickel particles.

Particle size distribution is often expressed as the cumulative distribution of a particle property. In addition, the cumulative distribution of particle size was calculated according to Equation (6):

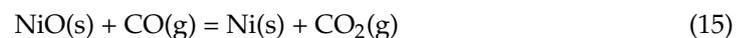
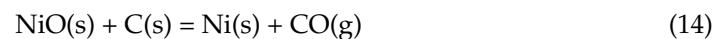
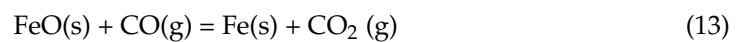
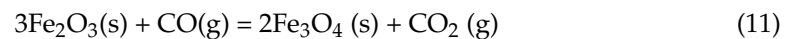
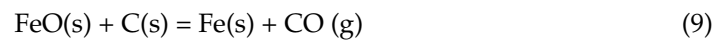
$$Q(D_i) = \frac{n(D < D_i)}{N} \times 100\% \quad (6)$$

where $Q(D_i)$ is the cumulative frequency, %; $n(D < D_i)$ is the number of ferronickel particles with size smaller than D_i ; and N is the total number of measured ferronickel particles.

3. Results and Discussion

3.1. Thermodynamic Analysis

The main reactions for the reduction of Fe_2O_3 and NiO to metallic Fe and Ni by carbothermic reduction were as follows:



To prove the thermodynamic feasibility of the Equation (7) to (15), their standard Gibbs free energy ($\Delta_r G_m^\ominus$) values with temperature (T) based on a fixed amount of reductive agent were calculated at 1 atmosphere by HSC Chemistry software (Version 6.0) [30,40]. The results were shown in Figure 3.

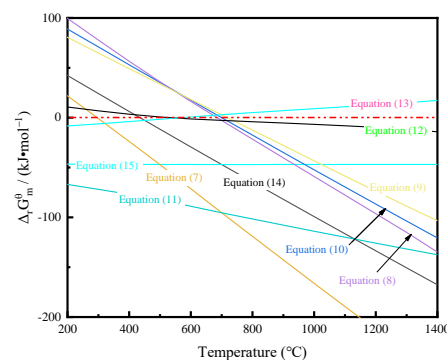


Figure 3. Gibbs free energy assessment as a function of temperature based on a fixed amount of reductive agent according to Equations (7)–(15).

It could be seen from Figure 3 that under the test temperature (1100–1400 °C), $\Delta_r G_m^\ominus$ of Equations (7)–(12), (14) and (15) were always negative. This indicated that the reactions of the iron and nickel oxides occurred spontaneously. When the temperatures were above 600 °C, $\Delta_r G_m^\ominus$ of Equation (13) was always positive, which indicated the reaction theoretically could not occur spontaneously at the test temperature. Since the $\Delta_r G_m^\ominus$ of the direct reduction (Equations (7)–(9) and (14)) was lower than that of the indirect reduction (Equations (11)–(13) and (15)) at temperatures above 700 °C, the former reactions were more likely to occur than the latter reactions. It could also be seen that nickel oxide could be reduced prior to iron oxides and Fe_2O_3 was reduced step by step to metallic iron. Further-

more, FeO was reduced to metallic iron by C as Equation (9) but was difficult to be reduced by CO. Therefore, sufficient C was required for the reduction of FeO to metallic iron.

3.2. Effect of Carbothermic Reduction Conditions on Size Characteristics of Ferronickel Particles

3.2.1. Effect of Anthracite Dosage

The effect of anthracite dosage on size characteristics of ferronickel particles was investigated under the following conditions: dosage of anthracite between 12 wt% and 24 wt%, carbothermic reduction temperature of 1200 °C, and carbothermic reduction time of 90 min. The experimental results are shown in Figure 4.

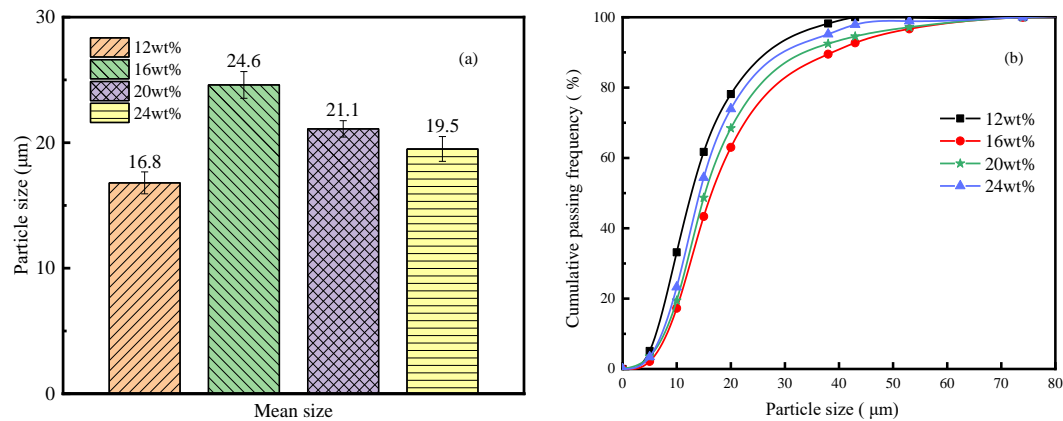


Figure 4. Effect of anthracite dosage on size characteristics of ferronickel particles: (a) mean size; (b) cumulative passing frequency distribution.

Figure 4a illustrates that the mean size of ferronickel particles slightly improved from 16.8 μm to 24.6 μm and then reduced to 21.1 μm, 19.5 μm as anthracite dosage increased, reporting that increasing appropriate anthracite dosage helped ferronickel particles agglomeration. Figure 4b shows that the curves of the cumulative passing frequency of ferronickel particles exhibited almost the same trend with respect to the particle size at various anthracite dosages. The cumulative passing frequency of each curve gradually improved with increasing ferronickel particle size. Especially, the cumulative passing frequency increased rapidly when the particle size reached a certain content. Furthermore, the curves of cumulative passing frequency systematically shifted rightward as anthracite dosage increased. In other words, under the same cumulative passing percentage, the corresponding ferronickel particle size increased with increasing anthracite dosage. For instance, D_{80} of ferronickel particles increased from 20.76 μm to 29.31 μm, and then reduced to 25.19 μm and 22.48 μm, respectively. When the amount of anthracite was 12 wt%, less nickel and iron oxides are reduced, so the particle size of ferronickel particles was smaller. When anthracite was added at 16 wt%, the reduction of nickel and iron oxides was promoted, so ferronickel particles continued to aggregate and grow. When the amount of anthracite was 20 wt%, the oxides of nickel and iron were further reduced, but the amount of nickel and iron oxides reacted with the gangue decreased, and the gangue containing nickel and iron usually had a low melting point. The reduction resulted in a restricted growth of ferronickel particles. When anthracite was increased to 24 wt%, on the one hand, the oxides of nickel and iron were further reduced, and on the other hand, more ash was brought in due to more anthracite. These two further inhibited the growth of ferronickel particles, so the particle size of ferronickel particles was further reduced [18].

The measurement results of the metallization degree of iron and nickel under different anthracite dosages showed that with the increase of anthracite dosage from 12 wt% to 24 wt%, the metallization degree of iron and nickel increased continuously. The metallization ratio of iron increased from 88.26% to 97.81%, and the metallization degree of nickel increased from 92.12% to 97.93%. The main reason was that the reducing atmosphere continued to strengthen. When the addition amount of anthracite was 12 wt%, the nickel

grade of the ferronickel product was 1.81 wt%, and the iron grade was 83.24 wt%. When the anthracite addition amount was 16 wt%, the nickel grade of the ferronickel product was 1.78 wt%, and the iron grade was 89.03 wt%. The nickel and iron grade of the ferronickel product was 1.76 wt% and 87.29 wt%, respectively, under the condition of adding 20 wt% anthracite. It could be seen that the index of the ferronickel product was the best when the addition amount of anthracite was 16 wt%, which was mainly caused by the larger particle size of ferronickel and the dissociation of gangue. This was consistent with the effect of the amount of anthracite on the particle size characteristics of ferronickel particles.

3.2.2. Effect of Carbothermic Reduction Temperature

Carbothermic reduction temperature affects the size characteristics of ferronickel particles. The different carbothermic reduction temperature experiments were conducted under the following conditions: anthracite dosage of 16 wt%, and carbothermic reduction time of 90 min. The experimental results are shown in Figure 5.

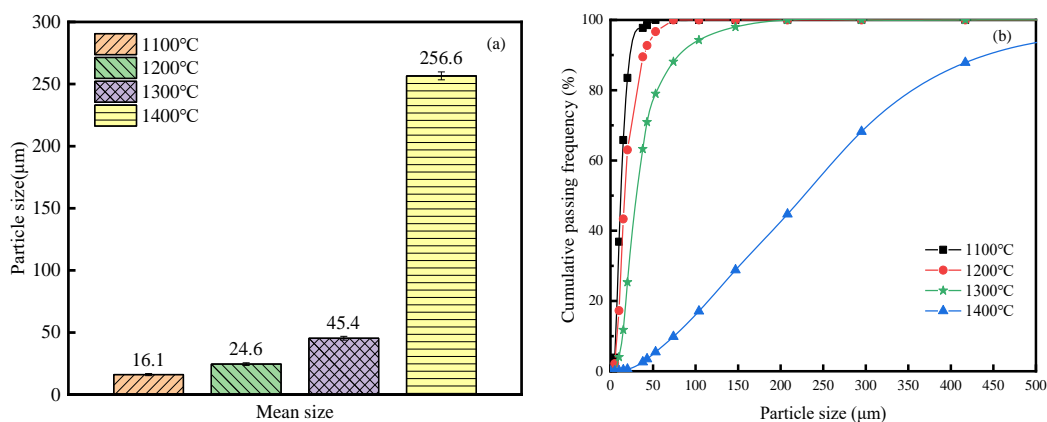


Figure 5. Effect of carbothermic reduction temperature on the size characteristics of ferronickel particles: (a) mean size; (b) cumulative passing frequency distribution.

Figure 5a depicts the mean size of ferronickel particles improved as carbothermic reduction temperature increased. When the carbothermic reduction temperature increased from 1100 °C to 1300 °C, the mean size of ferronickel particles grew slowly from 16.1 μm to 45.4 μm. However, when the carbothermic reduction temperature further increased to 1400 °C, the mean size raised markedly from 45.4 μm to 256.6 μm. As shown in Figure 5b, carbothermic reduction temperature has a strong effect on the cumulative passing frequency of ferronickel particles, particularly when the carbothermic reduction temperature was above 1300 °C. The curves of cumulative passing frequency shifted rightward as carbothermic reduction temperature increased. In other words, under the same cumulative passing percentage, the ferronickel particle size increased with increasing carbothermic reduction temperature. For example, D_{80} of ferronickel particles increased from 17.91 μm to 31.46 μm, 55.18 μm and 354.65 μm, respectively.

The coal-based reduction process of refractory ores can be divided into a nucleation stage and a particle growth stage [41]. When the carbothermic reduction temperature was between 1100 °C and 1200 °C, nickel and iron oxides were reduced to a metallic state then rapidly became ferronickel particle nucleus. However, the ferronickel particles were small due to the low particle diffusion ability. Besides, the formed fine ferronickel particles accounted for the majority and could not be effectively recovered in the subsequent grinding and magnetic separation processes. In contrast, when the carbothermic reduction temperature rose to 1400 °C, some gangue minerals with a low melting point started melting at temperatures above 1300 °C, which might increase the diffusion coefficient, improve migration ability, and therefore promote ferronickel particles agglomerated and consolidated to coarse ones. The growth rate in this stage might mainly be controlled by the

diffusion rate of ferronickel particles [42,43]. All these indicated that the number of large ferronickel particles grew with the increase of the carbothermic reduction temperature.

The determination results of the metallization degree of iron and nickel under different carbothermic reduction temperatures revealed that with the increase of carbothermic reduction temperature from 1100 °C to 1400 °C, the metallization degree of iron increased from 86.38% to 98.85%, and the metallization ratio of nickel increased from 91.05% to 98.97%. It showed that the increase of carbothermic reduction temperature was beneficial to the improvement of iron and nickel metallization degree. When carbothermic reduction temperature was 1100 °C, the nickel and iron grade of the ferronickel product was 1.75 wt% and 82.16 wt%, respectively. The nickel and iron grade of the ferronickel product was 1.72 wt% and 90.19 wt%, respectively, under the condition of carbothermic reduction temperature 1400 °C. The main reason was that with the increase of carbothermic reduction temperature, the size of ferronickel particles increased rapidly.

3.2.3. Effect of Carbothermic Reduction Time

The carbothermic reduction time of nickel laterite ore and red mud exhibited influence on the size of ferronickel particles. At anthracite dosage of 16 wt%, and carbothermic reduction temperature of 1400 °C, the different carbothermic reduction time experiments were conducted. The results are shown in Figure 6.

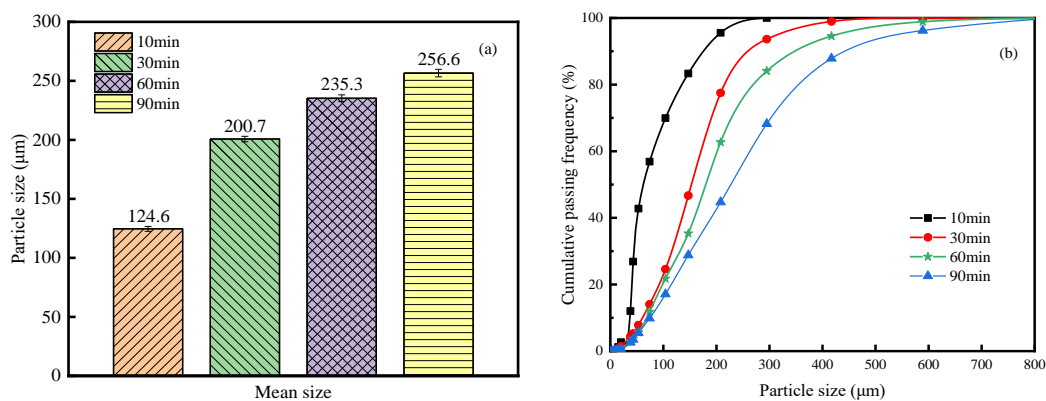


Figure 6. Effect of carbothermic reduction time on size characteristics of ferronickel particles: (a) mean size; (b) cumulative passing frequency distribution.

Figure 6a illustrates that the mean size of ferronickel particles gradually increased from 124.6 μm to 256.6 μm as the carbothermic reduction time extended from 10 min to 90 min, revealing that prolonging the time led to the larger mean sizes of ferronickel particles. Figure 6b presents the cumulative passing frequency increased with increasing particle size. When the carbothermic reduction time was 10 min, the growth rate of ferronickel particles was slow and the main proportion was occupied by small particles. With the carbothermic reduction time exceeded, the curves of cumulative passing frequency shifted to the right as carbothermic reduction time improved in the entire range. As an illustration, D_{80} of ferronickel particles increased from 135.88 μm to 217.67 μm, 257.82 μm, and 354.65 μm respectively. This result also showed that the number of ferronickel particles in large size increased with prolonging carbothermic reduction time. When the carbothermic reduction time was 10 min, the reduction of oxides of nickel and iron was insufficient, so the particle size of ferronickel particles was small. When the carbothermic reduction time was extended to 30 min, the nickel and iron oxides were further reduced, and the growth of ferronickel particles was promoted. When the carbothermic reduction time was further increased to 90 min, the ferronickel particles were further grown. Compared with 60 min, the particle size of ferronickel particles has become larger.

The metallization ratio of iron and nickel under different carbothermic reduction time was measured. When carbothermic reduction time was prolonged from 10 min to 90 min,

the metallization ratio of iron improved from 81.25% to 98.92%, and the metallization degree of nickel increased from 82.43% to 98.98%. The results showed that the increase of carbothermic reduction time was beneficial to the improvement of iron and nickel metallization degree. When carbothermic reduction time was 10 min, the nickel and iron grade of the ferronickel product was 1.74 wt% and 83.48 wt%, respectively. When carbothermic reduction time was prolonged to 90 min, the nickel and iron grade of the ferronickel product was 1.70 wt% and 91.01 wt%, respectively. It showed that the extension of carbothermic reduction time made the size of ferronickel particles larger, which was beneficial to the recovery of ferronickel.

3.3. Effect of Carbothermic Reduction Conditions on Grindability of Reduction Products

To characterize the relationship between the grindability and the carbothermic reduction variables, the anthracite dosage, the reduction temperature, and the reduction time were investigated in the following single factor experiments as displayed in Figure 7.

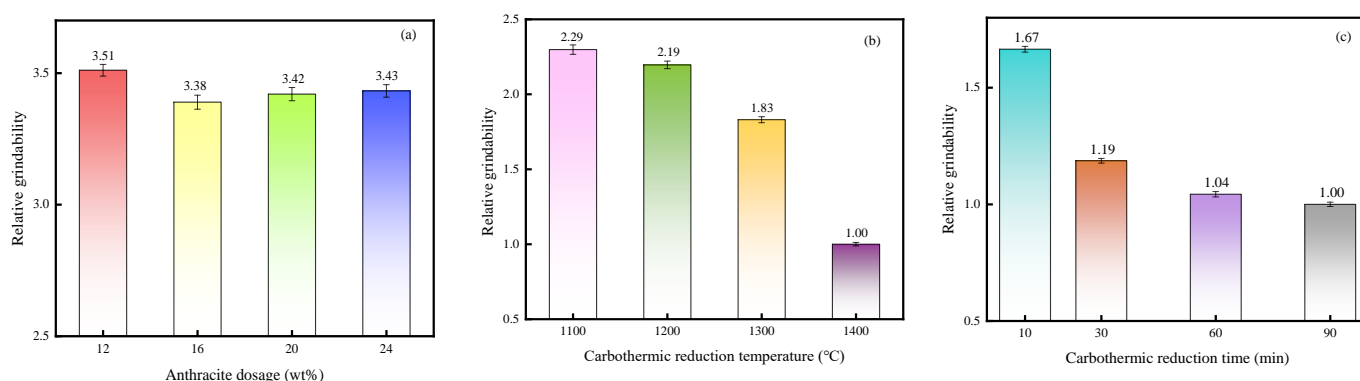


Figure 7. Relative grindability at various (a) anthracite dosage, (b) carbothermic reduction temperature, and (c) carbothermic reduction time.

Figure 7a shows that the G value of the carbothermic reduction products first decreased and then slightly improved as the anthracite dosage increased from 12 wt% to 24 wt%. The minimum G value reached 3.38 at 16 wt% anthracite dosages. The ferronickel particles were harder to be ground than gangue minerals under the same grinding conditions. When the amount of anthracite was 12 wt%, the reduction of nickel and iron oxides was insufficient. The average particle size of ferronickel particles was 16.8 μm and D_{80} of ferronickel particles was 20.76 μm . The G value of the carbothermic reduction products was high because of the small ferronickel particle size. When the amount of anthracite increased to 16 wt%, the oxides of nickel and iron were fully reduced. The average particle size of ferronickel particles increased to 24.6 μm and D_{80} of ferronickel particles increased to 29.31 μm . The particle size of ferronickel particles was large, so the G value of reduction products decreased. When anthracite was added at 20 wt%, the oxides of nickel and iron were fully reduced. However, the amount of nickel and iron oxides reacted with the gangue decreased. The average particle size of ferronickel particles was reduced to 21.1 μm and D_{80} of ferronickel particles was reduced to 25.19 μm . The G value of the reduction products is higher than that of anthracite with 16 wt%. When the amount of anthracite was 24 wt%, the oxides of nickel and iron were further fully reduced, the average particle size of ferronickel particles decreased to 19.5 μm , and D_{80} of ferronickel particles decreased to 22.48 μm . Due to the small particle size of ferronickel particles and easy grinding, the G value of the reduction products further increased.

Figure 7b shows that the carbothermic reduction temperature had a particularly significant effect on grindability of the co-reduction products. When the reduction temperature was 1100 $^{\circ}\text{C}$, the value of G constituted 2.29. As the reduction temperature increased from 1100 $^{\circ}\text{C}$ to 1400 $^{\circ}\text{C}$, the G value decreased sharply to 2.19, 1.83, and 1.00, indicating that grindability deteriorated with the reduction temperature rising. As the carbothermic reduc-

tion temperature increased from 1100 °C to 1400 °C, the reduction of nickel and iron oxides became more and more sufficient. The ferronickel particles grew rapidly, with an average particle size of 16.1 µm, 24.6 µm, 45.4 µm, and 256.6 µm, respectively. D_{80} of ferronickel particles were 17.91 µm, 31.46 µm, 55.18 µm, and 354.65 µm, respectively. The larger the particle size of ferronickel particles, the more difficult it was to grind, which was the reason why the relative grindability became worse with the increase of reduction temperature.

Similarly, Figure 7c shows that the G value gradually decreased from 1.67 to 1.00, namely, grindability also deteriorated with the reduction time prolonging from 10 min to 90 min. The main reason was that the reduction time was positively correlated with the particle size of ferronickel particles. When the reduction time was prolonged from 10 min to 90 min, the average particle size of ferronickel particles increased from 124.6 µm to 256.6 µm, and the D_{80} of ferronickel particles increased from 135.88 to 354.65 µm. Large-sized ferronickel particles were difficult to grind, resulting in a decrease in relative grindability with increasing reduction time.

3.4. Orthogonal Experiments

The L16(4^5) orthogonal experiment is shown in Table 2. The statistical results of the orthogonal experiments are shown in Figure 8 and Table 3.

Table 2. Orthogonal table.

Test No.	Factors		
	Anthracite Dosage (wt%)	Temperature (°C)	Time (min)
1	12	1100	10
2	12	1200	30
3	12	1300	60
4	12	1400	90
5	16	1100	30
6	16	1200	10
7	16	1300	90
8	16	1400	60
9	20	1100	60
10	20	1200	90
11	20	1300	10
12	20	1400	30
13	24	1100	90
14	24	1200	60
15	24	1300	30
16	24	1400	10

Figure 8 depicted the average value of each factor at each level. The effect of anthracite dosage, reduction temperature, and reduction time on size characteristics and relative grindability was consistent with the single factor test results. Likewise, the average value of reduction temperature changed the most than that of anthracite coal consumption and reduction time. The specific influence degrees for different factors can be seen in Table 3. It should be noted that the larger the range difference proves that the factor has a greater degree of influence on the corresponding evaluation indexes. Taking the evaluation index mean size as an example, $R\beta = 152.67 > R\alpha = 35.86 > R\gamma = 30.19$, indicating the affecting order on the mean size of ferronickel particle was roasting temperature, anthracite dosage, and roasting time. The highest mean size level was $\alpha 2\beta 4\gamma 3$, whose anthracite dosage, reduction temperature, and reduction time and was 16 wt%, 1400 °C, 60 min and, respectively. While the minimum was $\alpha 1\beta 1\gamma 1$, whose anthracite dosage, reduction temperature, and reduction time and was 12 wt%, 1100 °C, and 10 min respectively. The results of all evaluation indicators showed $\beta > \alpha > \gamma$ was the most important combination of factors. The reduction temperature, as the most influential factor, has a dominant

effect on the size characteristic and relative grindability followed by anthracite dosage and reduction time.

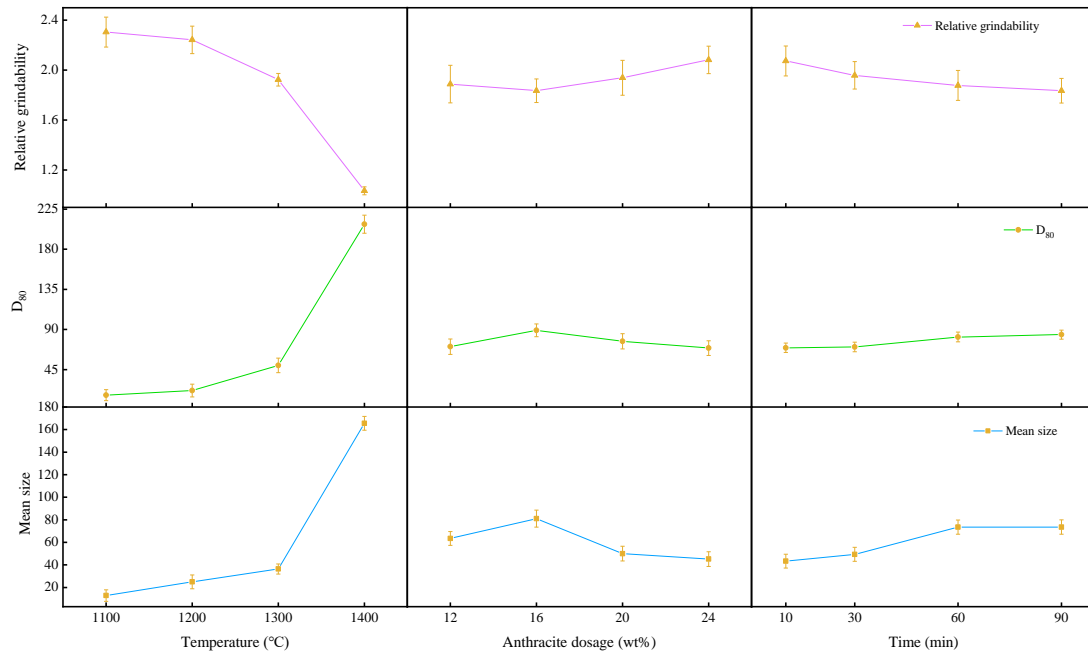


Figure 8. The average value at each level of each factor.

Table 3. Range analysis of different evaluation indexes.

Results	Range Analysis	Evaluation Indexes	
		Max	Min
Mean size	$R_{\beta} = 152.67 > R_{\alpha} = 35.86 > R_{\gamma} = 30.19$	$\alpha_2\beta_4\gamma_3$	$\alpha_1\beta_1\gamma_1$
D ₈₀	$R_{\beta} = 192.80 > R_{\alpha} = 20.74 > R_{\gamma} = 14.75$	$\alpha_2\beta_4\gamma_3$	$\alpha_1\beta_1\gamma_1$
Relative grindability	$R_{\beta} = 1.033 > R_{\alpha} = 0.247 > R_{\gamma} = 0.239$	$\alpha_1\beta_1\gamma_1$	$\alpha_2\beta_4\gamma_3$

Note: For convenience of expression, α , β , and γ are used to represent the anthracite dosage, reduction temperature, and reduction time of co-reduction system in the paper.

3.5. Co-Reduction Mechanism Analysis

3.5.1. Mineral Transformation

XRD patterns of reduction products under different co-reduction conditions were used to analyze the mineral transformation, as given in Figure 9.

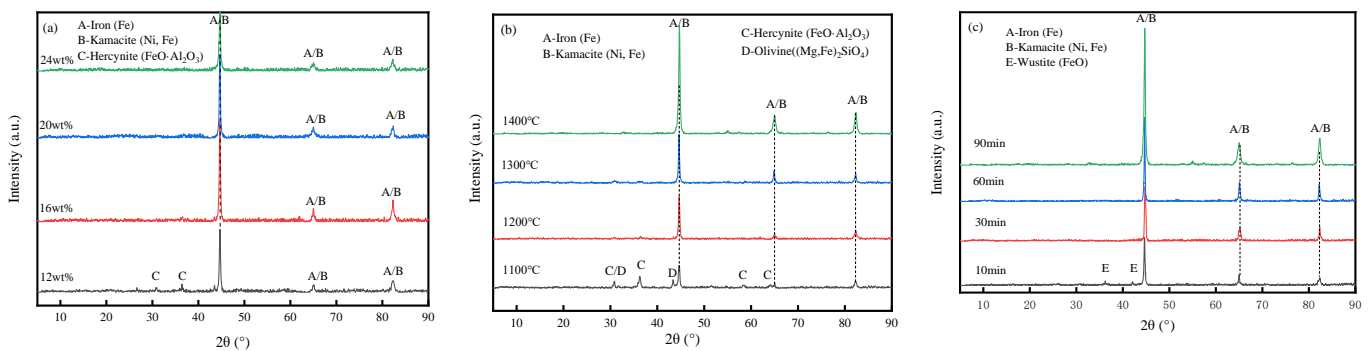


Figure 9. XRD patterns of reduction products: (a) different anthracite dosage, reduction temperature of 1200 °C, reduction time of 90 min; (b) different reduction temperature, anthracite of 16 wt%, reduction time of 90 min; (c) different reduction time, anthracite of 16 wt%, reduction temperature of 1400 °C.

As seen in Figure 9a, the phases mainly contained the diffraction peaks of iron and kamacite. However, when anthracite dosage was 12 wt%, the diffraction peaks of hercynite existed. This may be because when the anthracite dosage was 12 wt%, the reducing atmosphere provided was insufficient which prevented the reduction of iron-containing oxides to the metallic state, and therefore Al_2O_3 reacted with FeO and formed ferrous phases ($\text{FeO}\cdot\text{Al}_2\text{O}_3$) during the co-reduction process. When the anthracite dosage was increased from 12 wt% to 16 wt%, the diffraction peak hercynite decreased while that of iron and kamacite enhanced. This indicated that increasing anthracite dosage could strengthen the reactions of nickel and iron phases, which would be crucial for improving the recovery of nickel and iron in the subsequent magnetic separation process. When the anthracite dosage exceeded 16 wt%, the diffraction peak of kamacite and iron dropped slightly, this may be due to the fact that complete reduction of nickel-bearing and iron-bearing oxides in the raw materials had finished, and excessive carbon in anthracite was adverse for improving co-reduction effects.

The reduction temperature is the most significant factor in the co-reduction process based on previous research. As shown in Figure 9b, when the reduction temperature was 1100 °C, the main phases were kamacite, iron, hercynite, and olivine. The diffraction peaks of iron-bearing gangue minerals were relatively high, therefore, low reduction temperature resulted in lower iron recovery. As the temperature increased from 1200 °C to 1400 °C, the diffraction peak of kamacite and iron increased obviously while that of hercynite and olivine gradually disappeared, indicating that increasing the temperature promoted the reduction of hercynite and olivine. Additionally, the increased diffraction peak of kamacite indicated that more and more ferronickel particles were formed. Gangue particles were quite less, therefore, their diffraction peaks could not be seen in the XRD patterns. Under the same grinding conditions, ferronickel particles were more difficult to be ground than gangue ones thus the grindability deteriorated with the reduction temperature improved.

As shown in Figure 9c, when the reduction time was 10 min, wustite existed due to the reduction time being too short and the incomplete reduction reaction. The diffraction peak of wustite in the co-reduction product disappeared after reduction time was extended to 30 min. Also, the diffraction peak of kamacite and iron enhanced with the extension of reduction time. Clearly, the diffraction peak of kamacite and iron at the reduction time of 90 min had the highest intensity and the smallest half-peak width, indicating that the crystallization of the corresponding co-reduction product was relatively good.

Consequently, raising reduction temperature, prolonging reduction time and increasing appropriate anthracite dosage led to more nickel-bearing and iron-bearing minerals being reduced to a metallic state, which was more difficult to be ground.

3.5.2. Magnetic Properties

The magnetic moment and specific magnetic susceptibility of mixed raw material, reduction products obtained at various reduction conditions are given in Figure 10. As for the mixed raw material, the magnetic moment had been creeping up and was nearly linear with the magnetic field intensity (Figure 10a), and the curve of specific magnetic susceptibility increased to the highest point of $0.563 \times 10^{-4} \text{ m}^3 \cdot \text{kg}^{-1}$ then declined slightly (Figure 10b). The results indicated that the mixed raw material was weakly magnetic [44,45]. After co-reduction, the magnetic moment of each reduction product sharply increased with magnetic field intensity and then became flattening (Figure 10a,c,e). Moreover, the specific magnetic susceptibility increased sharply and peaked at $4.237\sim 10.494 \times 10^{-4} \text{ m}^3 \cdot \text{kg}^{-1}$, before decreasing sharply and flattening (Figure 10b,d,f). These results indicated that the reduction product was strongly magnetic compared to the mixed raw material, which could be effectively separated in subsequent magnetic separation. Indeed, increasing anthracite dosage, improving reduction temperature, and extending reduction time were all conducive to increasing the magnetic moment and the specific magnetic susceptibility. This is because nickel-containing minerals and iron-bearing minerals in the raw materials were mostly converted into kamacite and metallic iron according to the phase analysis result.

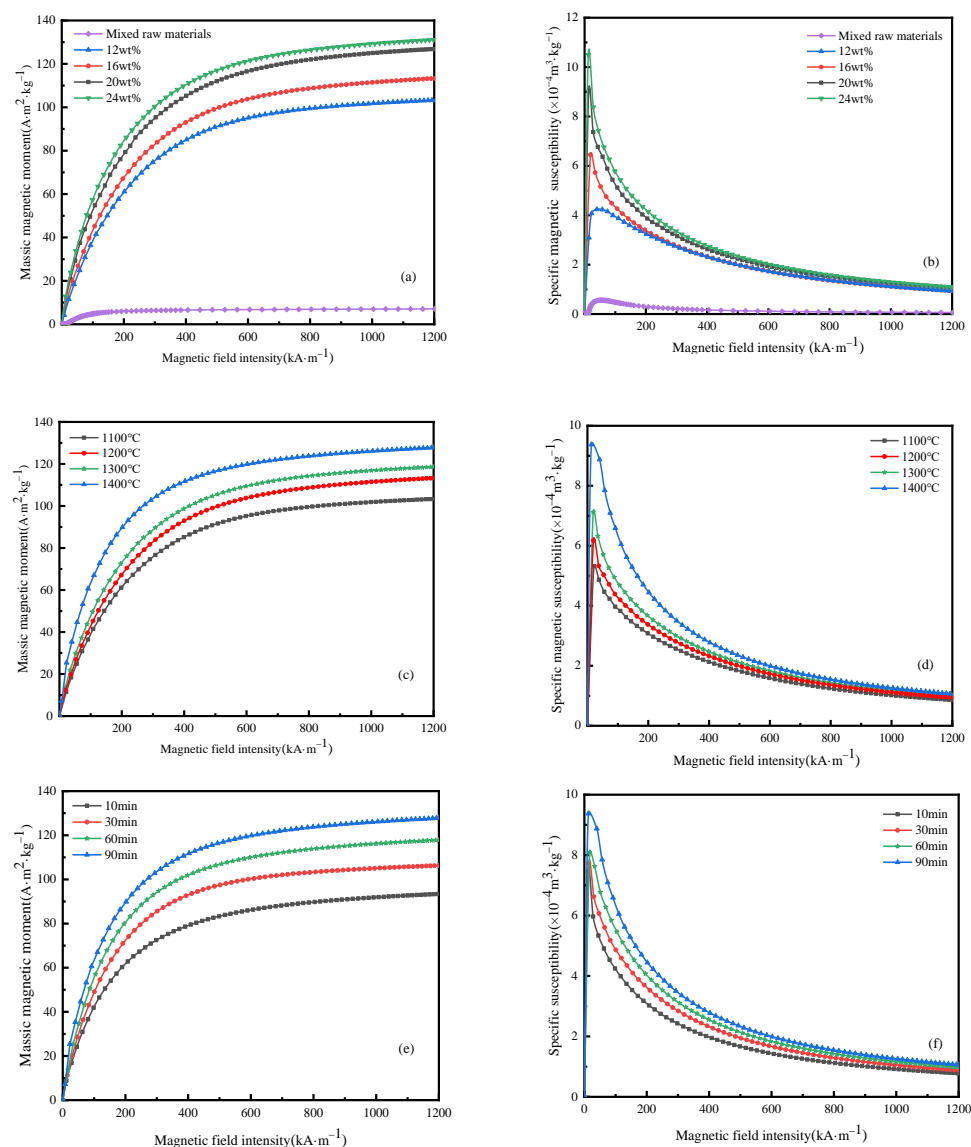


Figure 10. Magnetic moment (a,c,e) and specific magnetic susceptibility (b,d,f) of mixed raw material and reduction products obtained at various reduction conditions: (a,b) anthracite dosage; (c,d) reduction temperature; (e,f) reduction time.

3.5.3. Microstructure

The SEM images were presented in Figure 11 to better understand the growth behaviors of the ferronickel particles in the reduction products under different anthracite dosages. The typical elements composition of co-reduction product for areas in Figure 11 was shown in Table 4.

Table 4. EDS analysis results of co-reduction product for areas in Figure 11.

Anthracite Dosage (wt%)	No.	Element Composition (wt%)					Mineral Phases
		C	O	Al	Ni	Fe	
12	1	2.81	-	-	2.25	94.18	Kamacite
	2	2.03	35.12	30.95	-	31.90	Hercynite
16	3	2.97	-	-	2.17	95.02	Kamacite
20	4	3.33	-	-	1.92	94.75	Kamacite
24	5	3.77	-	-	2.11	94.12	Kamacite

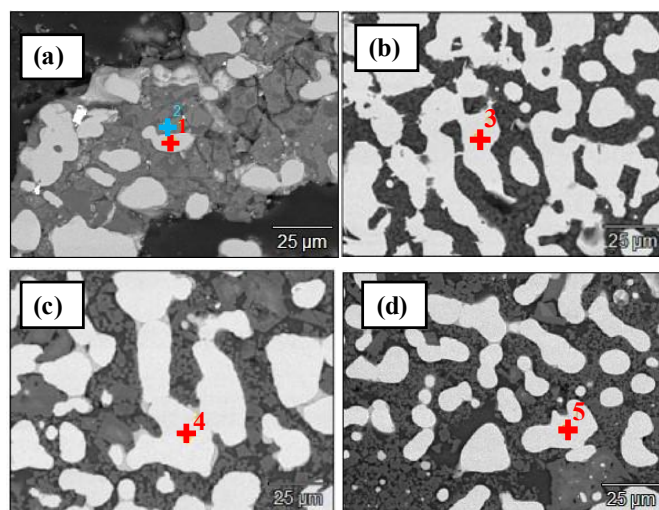


Figure 11. SEM images of ferronickel particles of reduction products at various anthracite dosage: (a) 12 wt%; (b) 16 wt%; (c) 20 wt%; (d) 24 wt%.

Ferronickel grains in Figure 11 existed in various irregular shapes with sizes between 5 μm to 50 μm . With the increase of anthracite dosage, the particle size of ferronickel particles increased slowly. In Figure 11a, when 12 wt% anthracite was added, the ferronickel grains in the co-reduction product were relatively small. From the EDS analysis in Table 4, the main components of point 1 were Fe and Ni. The main elements in point 2 were Fe, Al, and O, which were determined to be hercynite. As seen from Figure 11b, the ferronickel particles grew and the ferronickel particles included in the silicate minerals formed were reduced. The point of 4 and 5 in Table 4 showed the contents of C in the corresponding ferronickel particles were much higher than those in the ferronickel grains using less anthracite (points 1 and 3), which possibly hindered the fusion of ferronickel grains to clusters.

The SEM of the co-reduction products under different reduction temperatures at an anthracite dosage of 16 wt% and reduction time of 90 min is shown in Figure 12. The typical elements composition of co-reduction product for areas in Figure 12 are shown in Table 5.

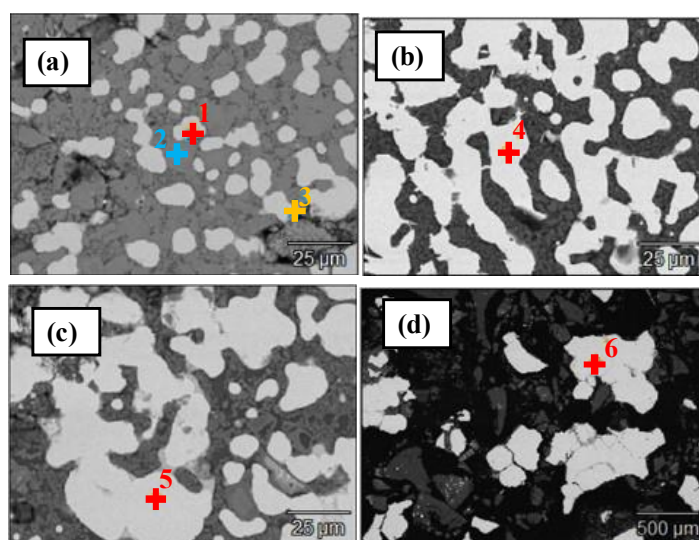


Figure 12. SEM images of ferronickel particles from different reduction temperature co-reduction products: (a) 1100 $^{\circ}\text{C}$; (b) 1200 $^{\circ}\text{C}$; (c) 1300 $^{\circ}\text{C}$; (d) 1400 $^{\circ}\text{C}$.

Table 5. EDS analysis results of reduction product for areas in Figure 12.

Temperature	No.	Element Composition (wt%)							Mineral Phases
		C	Fe	Ni	Si	Mg	O	Al	
1100 °C	1	2.57	94.09	1.99	-	-	-	1.37	Kamacite
	2	0.37	50.46	-	15.24	2.31	31.62	-	Olivine
	3	1.65	32.02	-	-	-	35.20	31.13	Hercynite
1200 °C	4	2.97	94.98	2.05	-	-	-	-	Kamacite
1300 °C	5	2.42	95.10	2.48	-	-	-	-	Kamacite
1400 °C	6	2.61	95.07	2.32	-	-	-	-	Kamacite

It can be seen from Figure 12 that as the reduction temperature continues to increase, the tendency of ferronickel particles to aggregate and grow became more obvious. When the temperature was 1100 °C, ferronickel grains separated from gangue matrix, and these fine new particles were mainly produced in the quasi-spherical shape (Figure 12a), which was consistent with the surface energy theory that the particle surface must be intrinsically less energetic. With reduction temperature improved, the rate of diffusion strengthened and the above fine ferronickel particles with high interfacial energy were propelled to contact the adjacent large particle boundary. Thus, the movement of particle boundaries made the particles grow continuously [46]. Small ferronickel particles agglomerated together to stack into chained ferronickel grains (Figure 12b,c). These chained ferronickel particles were moved and formed an accumulated bulk ferronickel particle cluster under 1400 °C in the size between 100 µm and 1000 µm. The main elements of point 2 in Table 5 were Mg, Fe, Si, and O, and analysis showed that it was olivine. Meanwhile, the peak of impurity elements such as Al existed in the ferronickel particles (seen Table 5 point 1), indicating that the ferronickel grains were composed of a small amount of gangue impurities. However, these impurities in ferronickel particles disappeared when the reduction temperature was from 1200 °C to 1400 °C, which indicated that the purity of ferronickel particles increased with the improvement of reduction temperature.

Figure 13 depicts the SEM micrographs of the co-reduction products at an anthracite dosage of 16 wt% and reduction temperature of 1400 °C with various reduction times, and Table 6 shows the typical elements composition of co-reduction product for areas in Figure 13.

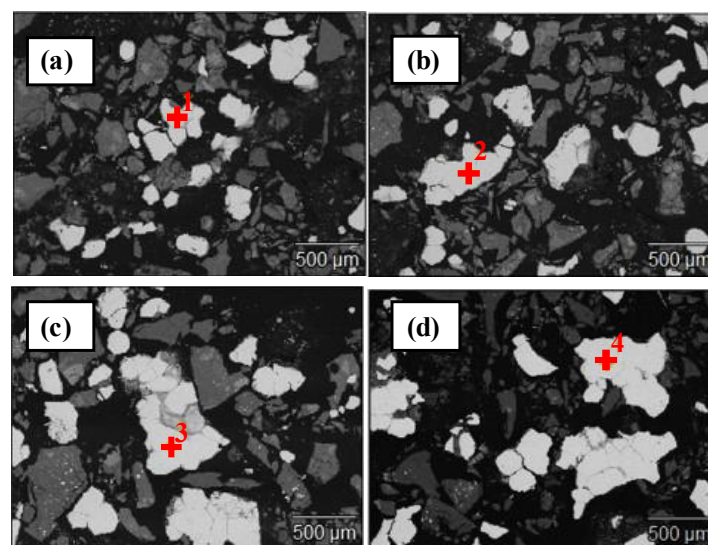
**Figure 13.** SEM images of ferronickel particles from different reduction time co-reduction products: (a) 10 min; (b) 30 min; (c) 60 min; (d) 90 min.

Table 6. EDS analysis results of reduction product for areas in Figure 13.

Time	No.	Element Composition (wt%)			Mineral
		C	Fe	Ni	Phases
10 min	1	3.57	94.18	2.25	Kamacite
30 min	2	2.81	95.02	2.17	Kamacite
60 min	3	1.40	95.68	2.92	Kamacite
90 min	4	1.09	96.08	2.83	Kamacite

The results in Figure 13 present that the ferronickel particles gradually increased with the prolongation of reduction time. When the duration was 10 min, the size of ferronickel particles was approximately 150 μm (Figure 13a) and these particles would become nuclei for grain growth. Further extended the reduction time to 30 min, ferronickel particles agglomerated and merged into bulk ferronickel grains under the function of interface energy and concentration gradient. The continuous migration and diffusion of chained ferronickel particles to the edge of the particle itself or the edge of the inner cavity promoted the formation of accumulated ferronickel particle clusters by extending the reduction duration to 90 min. Further analysis of the energy spectrum showed that ferronickel grains were relatively pure when extended the reduction time.

4. Conclusions

- (1) The mean size of ferronickel particles increased and the proportion of coarse particles grew as reduction temperature was increased, anthracite dosage was improved appropriately, or reduction time was extended. The relationships between co-reduction conditions and ferronickel particle size indicated a possibility of quality control of ferronickel products during co-reduction processes of laterite ore and red mud.
- (2) The relative grindability of the reduction products deteriorated as reduction temperature increased, or reduction time extended. The relative grindability of co-reduction products is negatively correlated to the ferronickel particle size. Reduction temperature has the most dominant effect on the size characteristic of ferronickel particles and relative grindability of the reduction products, followed by anthracite dosage and reduction time.
- (3) Raising reduction temperature, increasing appropriate anthracite dosage led to more nickel-bearing and iron-bearing minerals being reduced to a metallic state, which was more difficult to be ground. The fine ferronickel particles produced gradually agglomerated and consolidated into chained and even accumulated bulk clusters under the function of interface energy and concentration gradient with prolonging reduction time.

Author Contributions: Validation, formal analysis, writing—original draft preparation, X.G.; conceptualization, methodology, writing—review and editing, Z.L.; resources, investigation, data curation, Z.W.; writing—review and editing, T.S. All authors have read and agreed to the published version of the manuscript.

Funding: This research was funded by the National Nature Science Foundation of China, grant number 51874017, 52174236.

Conflicts of Interest: The authors declare no conflict of interest.

References

1. Zhu, D.Q.; Pan, L.T.; Guo, Z.Q.; Pan, J.; Zhang, F. Utilization of limonitic nickel laterite to produce ferronickel concentrate by the selective reduction-magnetic separation process. *Adv. Powder Technol.* **2019**, *30*, 451–460. [[CrossRef](#)]
2. Johnson, J.; Reck, B.K.; Wang, T.; Graedel, T.E. The energy benefit of stainless steel recycling. *Energ. Policy* **2007**, *36*, 181–192. [[CrossRef](#)]
3. Yang, T.; Li, X.M.; Zhao, J.X.; Cui, Y.R.; Xie, G.; Rao, Y.B. Status and research progress of Laterite nickel ore. *Nonferrous Met. Extr. Metall.* **2015**, *6*, 9–13.

4. Petrus, H.T.B.M.; Putera, A.D.P.; Sugiarto, E.; Perdana, I.; Warmada, I.W.; Nurjaman, F.; Astuti, W.; Mursito, A.T. Kinetics on roasting reduction of limonitic laterite ore using coconut-charcoal and anthracite reductants. *Miner. Eng.* **2019**, *132*, 126–133. [[CrossRef](#)]
5. Zhang, Y.Y.; Cui, K.K.; Wang, J.; Wang, X.F.; Qie, J.M.; Xu, Q.Y.; Qi, Y.H. Effects of direct reduction process on the microstructure and reduction characterization of carbon-bearing nickel laterite ore pellets. *Powder Technol.* **2020**, *376*, 496–506. [[CrossRef](#)]
6. Ma, B.Y.; Wu, H.; Gao, Z. Research development on treatment processes of laterite nickel ore. *Refract. Lime* **2022**, *47*, 35–40.
7. Tong, L.B.; Klein, B.; Zanin, M.; Quast, K.; Skinner, W.; Addai-Mensah, J.; Robinson, D. Stirred milling kinetics of siliceous goethitic nickel laterite for selective comminution. *Miner. Eng.* **2013**, *49*, 109–115. [[CrossRef](#)]
8. Zhang, Z.H.; Mao, Y.J. The current situation of the technology of nickel laterite. *Hunan Nonferrous Met.* **2012**, *28*, 31–35.
9. Yang, Z.Y.; Zhang, W.; Shen, Y.F.; Wang, L.; Li, H. Current status of smelting process of laterite nickel ore. *China Nonferrous Metall.* **2020**, *4*, 1–6.
10. Rubisov, D.H.; Papangelakis, V.G. Sulphuric acid pressure leaching of laterites—a comprehensive model of a continuous autoclave. *Hydrometallurgy* **2000**, *58*, 89–101. [[CrossRef](#)]
11. Mainak, M.; Lars, S. Structure and elasticity of serpentinite at high pressure. *Earth Planet. Sci. Lett.* **2009**, *297*, 11–19.
12. Liu, K.; Chen, Q.; Hu, H. Comparative leaching of minerals by sulphuric acid in a Chinese ferruginous nickel laterite ore. *Hydrometallurgy* **2009**, *98*, 281–286. [[CrossRef](#)]
13. Guo, X.; Shi, W.T.; Dong, L.I. Leaching behavior of metals from limonitic laterite ore by high pressure acid leaching. *Trans. Nonferrous Met. Soc. China* **2011**, *21*, 191–195. [[CrossRef](#)]
14. McDonald, R.; Whittington, B. Atmospheric acid leaching of nickel laterites review. *Hydrometallurgy* **2008**, *91*, 35–55. [[CrossRef](#)]
15. Zhao, J.F. Treatment for Myanmar nickel laterite with RKEY process. *Nonferrous Met. Extr. Metall.* **2013**, *1*, 8–11.
16. Jiang, M.; Sun, T.C.; Liu, Z.G.; Zhang, S.Y.; Liu, N.; Kou, J.; Cao, Y.Y. Phase transformation of nickel laterite ores in the selective reduction roasting process. *J. Univ. Sci. Technol. Beijing* **2013**, *35*, 27–34.
17. Zhang, Y.Y.; Zhao, J.; Ma, X.L.; Li, M.Y.; Lv, Y.; Gao, X.D. Isothermal reduction kinetics and mechanism of pre-oxidized ilmenite. *Min. Metall. Explor.* **2019**, *36*, 825–837. [[CrossRef](#)]
18. Zhou, S.W.; Dong, J.C.; Lu, C.; Li, B.; Li, F.; Zhang, B.; Wang, H.; Wei, Y.G. Effect of sodium carbonate on phase transformation of high-magnesium laterite ore. *Mater. Trans.* **2017**, *58*, 790–794. [[CrossRef](#)]
19. Luo, J.; Li, G.H.; Peng, Z.W.; Rao, M.J.; Zhang, Y.B.; Jiang, T. Phase evolution and Ni-Fe granular growth of Saproplitic Laterite Ore-CaO mixtures during reductive roasting. *JOM* **2016**, *68*, 3015–3021. [[CrossRef](#)]
20. Lv, X.M.; Lv, W.; Liu, M.; You, Z.X.; Lv, X.W.; Bai, C.G. Effect of sodium sulfate on preparation of ferronickel from nickel laterite by carbothermal reduction. *ISIJ Int.* **2018**, *58*, 799–805. [[CrossRef](#)]
21. Wu, S.C.; Li, Z.Y.; Sun, T.C.; Li, X.H.; Xu, C.Y. Effect of calcium compounds on direct reduction and phosphorus removal of high-phosphorus iron ore. *J. Cent. South Univ.* **2022**, *29*, 443–454. [[CrossRef](#)]
22. Nath, H.; Sahoo, P.; Sahoo, A. Characterization of red mud treated under high temperature fluidization. *Powder Technol.* **2015**, *269*, 233–239. [[CrossRef](#)]
23. Liu, X.; Han, Y.; He, F.; Gao, P.; Yuan, S. Characteristic, hazard and iron recovery technology of red mud—A critical review. *J. Hazard. Mater.* **2021**, *420*, 126542. [[CrossRef](#)]
24. Liu, W.C.; Yang, J.K.; Xiao, B. Review on treatment and utilization of bauxite residues in China. *Int. J. Miner. Process.* **2009**, *93*, 220–231. [[CrossRef](#)]
25. Komnitsas, K.; Bartzas, G.; Paspaliaris, I. Efficiency of limestone and red mud barriers: Laboratory column studies. *Miner. Eng.* **2004**, *17*, 183–194. [[CrossRef](#)]
26. Reddy, P.S.; Reddy, N.G.; Serjun, V.Z.; Mohanty, B.; Das, S.K.; Reddy, K.R.; Rao, B.H. Properties and assessment of applications of red mud (bauxite residue): Current status and research needs. *Waste Biomass Valoriz.* **2021**, *12*, 1185–1217. [[CrossRef](#)]
27. Liu, X.M.; Zhang, N. Utilization of red mud in cement production: A review. *Waste Manag. Res.* **2011**, *29*, 1053–1063. [[CrossRef](#)]
28. He, A.P.; Zeng, J.M. Direct preparation of low Ni-Cr alloy cast iron from red mud and laterite nickel ore. *Mater. Des.* **2017**, *115*, 433–440. [[CrossRef](#)]
29. Wang, X.P.; Sun, T.C.; Kou, J.; Li, Z.C.; Tian, Y. Feasibility of co-reduction roasting of a saprolitic laterite ore and waste red mud. *Int. J. Min. Met. Mater.* **2018**, *25*, 591–597. [[CrossRef](#)]
30. Guo, X.S.; Li, Z.Y.; Han, J.C.; Yang, D.; Sun, T.C. Study of straw charcoal as reductant in co-reduction roasting of laterite ore and red mud to prepare powdered ferronickel. *Min. Metall. Explor.* **2021**, *38*, 2217–2228. [[CrossRef](#)]
31. Gao, L.H.; Liu, Z.G.; Pan, Y.Z.; Ge, Y.; Feng, C.; Chu, M.S.; Tang, J. Separation and recovery of iron and nickel from low-grade laterite nickel ore using reduction roasting at rotary kiln followed by magnetic separation technique. *Min. Metall. Explor.* **2019**, *36*, 375–384. [[CrossRef](#)]
32. Guo, X.S.; Li, Z.Y.; Han, J.C.; Yang, D.; Sun, T.C. Petroleum coke as reductant in co-reduction of low-grade laterite ore and red mud to prepare ferronickel: Reductant and reduction effects. *Int. J. Miner. Metall. Mater.* **2022**, *29*, 455–463. [[CrossRef](#)]
33. Bartzas, G.; Komnitsas, K. Life cycle assessment of ferronickel production in Greece. *Resour. Conserv. Recycl.* **2015**, *105*, 113–122. [[CrossRef](#)]
34. Zulhan, Z.; Shalat, W. Evolution of ferronickel particles during the reduction of low-grade saprolitic laterite nickel ore by coal in the temperature range of 900–1250 °C with the addition of CaO–CaF₂–H₃BO₃. *Int. J. Miner. Metall. Mater.* **2021**, *28*, 612–620. [[CrossRef](#)]

35. Wang, X.P.; Sun, T.C.; Wu, S.C.; Chen, C.; Kou, J.; Xu, C.Y. A novel utilization of Bayer red mud through co-reduction with a limonitic laterite ore to prepare ferronickel. *J. Clean. Prod.* **2019**, *216*, 33–41. [[CrossRef](#)]
36. Guo, X.S.; Xu, C.Y.; Wang, Y.S.; Li, X.H.; Sun, T.C. Recovery of nickel and iron from low-grade laterite ore and red mud using co-reduction roasting: Industrial-scale test. *Physicochem. Probl. Miner. Process.* **2021**, *57*, 61–72. [[CrossRef](#)]
37. Petrakis, E.; Karmali, V.; Komnitsas, K. Factors affecting nickel upgrade during selective grinding of low-grade limonitic laterites. *Miner. Processing Extr. Metall.* **2021**, *130*, 192–201. [[CrossRef](#)]
38. Komnitsas, K.; Petrakis, E.; Pantelaki, O.; Kritikaki, A. Column Leaching of Greek Low-Grade Limonitic Laterites. *Minerals* **2018**, *8*, 377. [[CrossRef](#)]
39. García, G.G.; Oliva, J.; Guasch, E.; Anticoi, H.; Coello-Velázquez, A.L.; Menéndez-Aguado, J.M. Variability study of Bond work Index and grindability index on various critical metal ores. *Metals* **2021**, *11*, 970. [[CrossRef](#)]
40. Roine, A.; Kotiranta, T. Development of sustainable processes with new HSC Chemistry 6.0 software. In Proceedings of the European Metallurgical Conference, EMC 2007, Dusseldorf, Germany, 11–14 June 2007; Volume 4, pp. 1877–1888.
41. Sun, Y.S.; Han, Y.X.; Li, Y.F.; Li, Y.J. Formation and characterization of metallic iron grains in coal-based reduction of oolitic iron ore. *Int. J. Miner. Metall. Mater.* **2017**, *24*, 123–129. [[CrossRef](#)]
42. Sun, Y.S.; Han, Y.X.; Gao, P.; Ren, D.Z. Distribution behavior of phosphorus in the coal-based reduction of high-phosphorus-content oolitic iron ore. *Int. J. Miner. Metall. Mater.* **2014**, *21*, 331–338. [[CrossRef](#)]
43. Yuan, S.; Zhou, W.T.; Han, Y.X.; Li, Y.J. Selective enrichment of iron particles from complex refractory hematite-goethite ore by coal-based reduction and magnetic separation. *Powder Technol.* **2020**, *367*, 305–316. [[CrossRef](#)]
44. Luo, L.Q.; Zhang, X.X.; Wang, H.Y.; Zheng, B.T.; Wei, C.X. Comparing strategies for iron enrichment from Zn-and Pb-bearing refractory iron ore using reduction roasting-magnetic separation. *Powder Technol.* **2021**, *393*, 333–341. [[CrossRef](#)]
45. Jin, J.P.; Liu, X.; Yuan, S.; Gao, P.; Li, Y.J.; Zhang, H.; Meng, X.Z. Innovative utilization of red mud through co-roasting with coal gangue for separation of iron and aluminum minerals. *J. Ind. Eng. Chem.* **2021**, *98*, 298–307. [[CrossRef](#)]
46. Li, X.M.; Li, Y.; Xing, X.D. Particle growth characterization of metallic iron in direct coal-based reduction of nickel slag. *Iron Steel.* **2020**, *55*, 104–109.